Wake monochromator in asymmetric and symmetric Bragg and Laue geometry for self-seeding the European X-ray FEL

Gianluca Geloni, [a,1] Vitali Kocharyan [b] Evgeni Saldin [b]
Svitozar Serkez [b] and Martin Tolkiehn [b]

[a] *European XFEL GmbH, Hamburg, Germany*
[b] *Deutsches Elektronen-Synchrotron (DESY), Hamburg, Germany*

Abstract

We discuss the use of self-seeding schemes with wake monochromators to produce TW power, fully coherent pulses for applications at the dedicated bio-imaging bealine at the European X-ray FEL, a concept for an upgrade of the facility beyond the baseline previously proposed by the authors. We exploit the asymmetric and symmetric Bragg and Laue reflections (sigma polarization) in diamond crystal. Optimization of the bio-imaging beamline is performed with extensive start-to-end simulations, which also take into account effects such as the spatio-temporal coupling caused by the wake monochromator. The spatial shift is maximal in the range for small Bragg angles. A geometry with Bragg angles close to $\pi/2$ would be a more advantageous option from this viewpoint, albeit with decrease of the spectral tunability. We show that it will be possible to cover the photon energy range from 3 keV to 13 keV by using four different planes of the same crystal with one rotational degree of freedom.

1 Introduction

One of the highest priority for experiments at any advanced XFEL facility is to establish a beamline for studying biological objects at the mesoscale, including large macromolecules, macromolecular complexes, and cell organelles. This requires 2-6 keV photon energy range and TW peak-power pulses [1]-[5]. However, higher photon energies (up to 13 keV) are needed to reach the K-edges of commonly used elements, such as Se, for anomalous

[1] Corresponding Author. E-mail address: gianluca.geloni@xfel.eu

experimental phasing. Studies at intermediate resolutions need access to the water window at 0.5 keV. The pulse duration should be adjustable from 2 fs to 10 fs.

A basic concept and design of an undulator system for a dedicated bio-imaging beamline at the European XFEL was proposed in [6], and optimized in [7]. All the requirements in terms of photon beam characteristics can be satisfied by the use of a very efficient combination of self-seeding, fresh bunch and undulator tapering techniques [8]-[19]. In particular, a combination of self-seeding and undulator tapering techniques would allow to meet the design TW output power. The bio-imaging beamline would be equipped with two different self-seeding setups. For soft X-ray self-seeding, the monochromator consists of a grating [8]. Starting around the energy of 3 keV it is possible to use a single crystal (wake) monochromator instead of a grating [7].

In [7] we demonstrated that it will be possible to cover the photon energy range between 3 keV and 13 keV using the C(111), C(220) and C(004) symmetric Bragg reflections. In this scenario, three different crystals would enable self-seeding for the different spectral range. In particular, we proposed to exploit the C(111) symmetric Bragg reflection in the photon energy range between 3 keV and 5 keV.

While developing a design for the bio-imaging beamline, the authors first priority was to have it satisfying all requirements. Having achieved that goal, the next step is to optimize the design, making it as simple as possible. The design presented here aims for experimental simplification and cost reduction of the self-seeding setups. In order to improve the original design, here we propose to exploit asymmetric Bragg and Laue C(111), C(113) and C(333) reflections together with the symmetric Bragg reflection C(004). The novel design of the self-seeding setup combines a wide photon energy range with a much needed experimental simplicity. Only one diamond crystal is needed, and only one rotational degree of freedom is required.

While, in this article, we consider applications for the bio-imaging beamline in particular, the present study can also be applied to other beamlines, for example the SASE1-SASE2 lines at the European XFEL as well.

2 Dynamical diffraction theory and asymmetric-cut crystals

We begin our analysis of asymmetric-cut crystals by specifying the scattering geometry under study. With reference to Fig. 1, and following the notation in [20] we identify the crystal surface with the unit vector normal to the

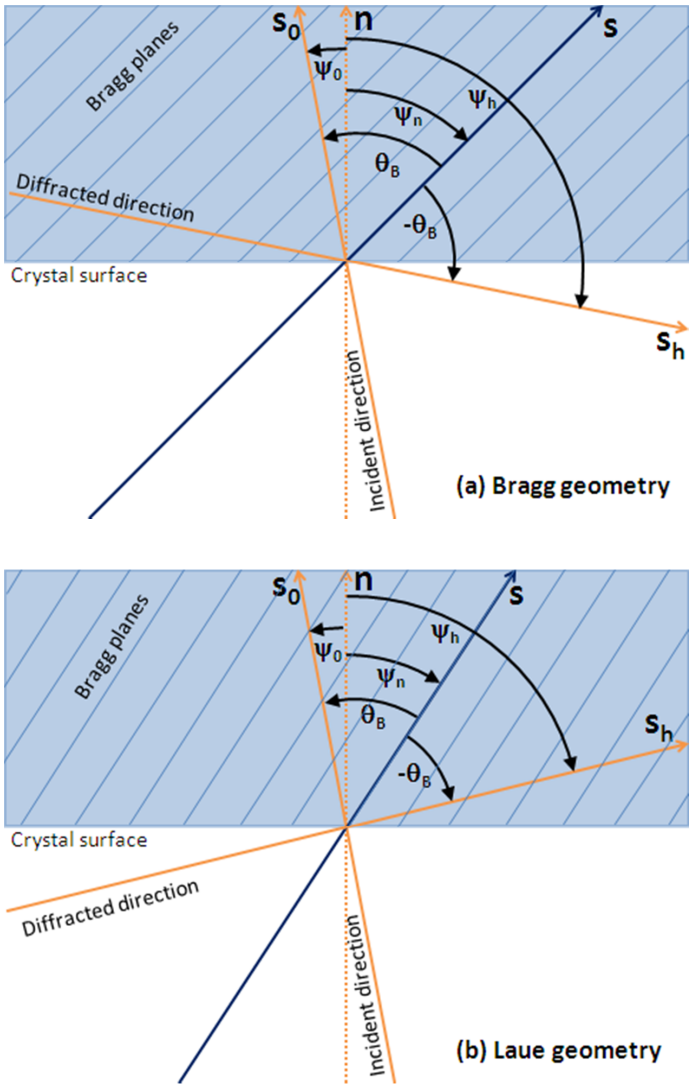

Fig. 1. Sketch of (a) Bragg and (b) Laue scattering geometry.

crystal surface $\vec{n}$, directed inside the crystal. The unit vector $\vec{s}$ indicates the trace of the Bragg planes. The direction of the incident beam is specified by the unit vector $\vec{s}_0$, while that of the diffracted beam is given by $\vec{s}_h$. Always following [20], we call ψ_n the angle between $\vec{n}$ and $\vec{s}$, ψ_0 the angle between $\vec{n}$ and $\vec{s}_0$, and ψ_h the angle between $\vec{n}$ and $\vec{s}$. The signs of these angles are univocally fixed by requiring that the angle between $\vec{s}$ and $\vec{s}_0$ is positive (and equal to the Bragg angle θ_B), while the angle between $\vec{s}$ and $\vec{s}_h$ is negative (and equal to -θ_B). Fig. 1 shows two generic examples for both Bragg and Laue geometries.

Let us consider an electromagnetic plane wave in the x-ray frequency range incident on an infinite, perfect crystal. Within the kinematical approxima-

tion, according to the Bragg law, constructive interference of waves scattered from the crystal occurs if the angles between the reflecting lattice planes and both incident and reflected beams are equal to Bragg angle θ_B, Fig. 1. The wavelength λ and the Bragg angle are related by the well known equation

$$\lambda = 2d \sin(\theta_B) \,, \tag{1}$$

where d is the distance between Bragg planes, and from now on we assume reflection into the first order. This equation shows that for a given wavelength of the x-ray beam diffraction is possible only at certain angles determined by d. It is important to remember the following geometrical relationships:

- In the kinematical approximation, the Bragg reflection is a mirror reflection i.e. the angle between the incident X-ray beam and the normal to the Bragg planes is equal to that between the normal and the reflected beam.
- The incident beam and the forward diffracted (i.e. the transmitted) beam have the same direction.

Diffraction from an asymmetric-cut crystal is equivalent to diffraction from a blazed grating. This equivalence has already been noted in [21]. The Bragg-reflected light from an asymmetric-cut crystal behaves as the light diffracted from a grating with period $D = d/\cos(\psi_n)$ and is dispersed in accordance with the grating equation

$$\lambda = D[\sin(\psi_0) - \sin(\psi_h)] \,. \tag{2}$$

When the Bragg condition Eq. (1) and the mirror reflection condition are simultaneously met one obtains

$$\psi_0 = \psi_n + \theta_B \tag{3}$$

and

$$\psi_h = \psi_n - \theta_B \tag{4}$$

By direct substitution in Eq. (2) and using simple trigonometric relations, it is easy to check that Eq. (3) and Eq. (4) satisfy the grating equation.

We now turn our attention beyond the kinematical approximation to the dynamical theory of diffraction by a crystal. With reference to Fig. 1, let us define the angle between the crystal surface and the input beam as $\theta_i = \pi/2 - \psi_0$. Similarly, we define the diffracted angle $\theta_d = \pi/2 - \psi_h$, with θ_d a function of the frequency, according to Eq. (2). We also define the angle

between the Bragg planes and the crystal surface as $\alpha = \pi/2 - \psi_n$. All these new quantities follow the previously defined convention as concerns their signs. Note that Eq. (3) and Eq. (4) can be rewritten in terms of incident and diffracted angles as $\theta_i = \alpha - \theta_B$ and $\theta_d = \alpha + \theta_B$.

It is useful to describe the modification of the incident beam by means of a transfer function. The reflectivity curve - the reflectance - can be expressed in the frame of dynamical theory as

$$R(\theta_i, \theta_d, \omega) = R[\Delta\omega + \omega_B \Delta\theta_i \cot(\theta_B), \Delta\theta_d] \,, \tag{5}$$

where $\Delta\omega = (\omega - \omega_B)$, $\Delta\theta_i = \theta_i - \theta_B + \alpha$, and $\Delta\theta_d = \theta_d - \theta_B - \alpha$ are, respectively, the deviations of frequency, incident angle and diffracted (i.e. reflected) angle from the resonance (Bragg) frequency and angles, respectively. The frequency ω_B and the angle θ_B are given by the Bragg law $\omega_B \sin(\theta_B) = \pi c/d$.

Consider now a perfectly collimated, white beam incident on the crystal. Within the kinematic approximation, the transfer function as a function of the first argument is a Dirac δ-function, $\delta[\Delta\omega + \omega_B \Delta\theta_i \cot(\theta_B)]$ which is another representation of the Bragg law in differential form:

$$\frac{d\lambda}{d\theta_i} = \lambda \cot(\theta_B) \,. \tag{6}$$

In addition to this, within the kinematic approximation, reflection from a lattice plane is always a mirror reflection, and

$$\frac{d\theta_d}{d\theta_i} = 1 \,. \tag{7}$$

Moving to the framework of the dynamical theory, and in contrast to what has just been said, the reflectivity width is finite. This means that there is a reflected beam even when the incident angle and the wavelength of the incoming beam are not exactly related by the Bragg equation. It is interesting to note that incident beam and transmitted beam continue to have the same direction also in the framework of dynamical theory. However, in the framework of the dynamical theory and in the case of asymmetric-cut crystal, the reflection from lattice planes are not a mirror reflection anymore: the grating equation Eq. (2), holds, and the reflection from the crystal surface is always a grating reflection.

The diffraction from the asymmetric-cut crystal in Bragg and Laue geometry can be described an asymmetry parameter, b, defined by

$$b = \frac{\vec{n} \cdot \vec{s_0}}{\vec{n} \cdot \vec{s_h}} = \frac{\cos(\psi_0)}{\cos(\psi_h)} \,. \tag{8}$$

In literature on X-ray crystal diffraction, the asymmetry parameter is sometimes defined as inverse of b, and indicated with the letter γ, for example in [20]. Here we follow the same convention used in [21]. Note that $|b| = \sigma_{\text{in}}/\sigma_{\text{out}}$ is the ratio of the widths of incident and diffracted beams. From Eq. (2) follows that

$$b = \frac{d\theta_d}{d\theta_i} \,. \tag{9}$$

As has been pointed out elsewhere, this is a consequence of Liouville theorem [21]. In fact, a quasi-monochromatic, collimated beam of finite width that is reduced in width must be dispersed in angle to preserve the space-angle phase volume.

For the Bragg geometry, where the diffracted light exists on the same side of the surface as the incident beam, we have $b < 0$, whereas $b > 0$ describes Laue geometry. In particular, $b = -1$ corresponds the symmetric Bragg diffraction, and $b = 1$ corresponds to the symmetric Laue diffraction.

The dispersion of the diffracted light from the asymmetric-cut crystal follows directly from the grating equation, yielding

$$\lambda \frac{d\theta_d}{d\lambda} = (1 + b) \tan(\theta_B) \,. \tag{10}$$

As expected, there is no dispersion for symmetric Bragg geometry ($b = -1$) because there is no grating structure in that case.

In the following, we will consider one single diamond crystal, as the 100 μm thick crystal proposed in [14], and currently used into the LCLS self-seeding setup [22]. We will define a cartesian reference system $\{x, y, z\}$ linked with the crystal. The direction z corresponds to the direction identified by the Miller indexes 0, 0, 1, which also coincides with the direction of $\vec{n}$, while x and y are specified as in Fig. 2, so that the direction [110] corresponds to the x direction.

The crystal can rotate freely around the y axis (pitch angle) as indicated in the figure. In this way, we can exploit several symmetric and asymmetric reflection: we will be able to cover the entire energy range between 3 keV and 13 keV by changing the pitch angle of the crystal in Fig. 2. In the low energy range between 3 keV and 5 keV we will use the C(111) asymmetric

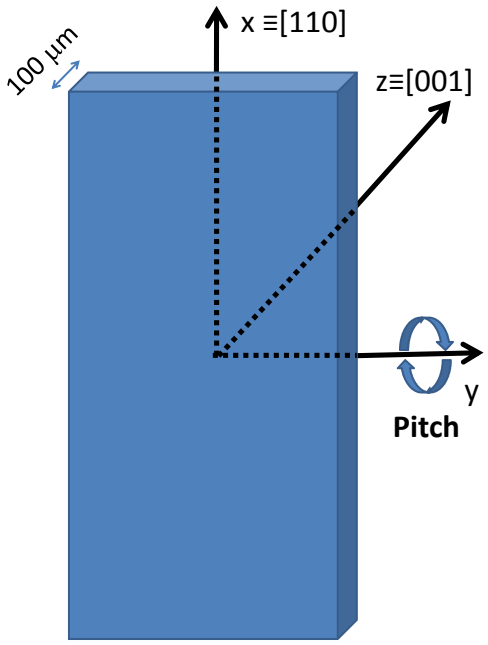

Fig. 2. Drawing of the orientation of the diamond crystal considered in this article.

Table 1
Useful Diamond Reflections

hkl	Min. Energy (keV)	ΔE (meV)
111	3.01034	192.0
311	5.76401	56.0
400	6.95161	60.6
333	9.03035	27.3
444	12.0404	25.0

reflection (in Bragg or Laue geometry, depending on the energy). At higher energies between 5 keV and 7 keV we propose to go to the C(113) asymmetric reflection in Bragg geometry. In the range between 7 keV and 9 keV we can use instead the C(004) symmetric reflection, in Bragg geometry. Finally, for energies larger than 9 keV we propose the use of the C(333) asymmetric reflection, in Bragg geometry [2]. The list of reflections considered in this article is summarized in Table 1, extracted from [23].

[2] It should be remarked that above 12 keV the C(444) asymmetric Bragg reflection turns out to be a valid alternative, though results are not explicitly analyzed in this article. The Bragg angle is, in this case, very near to $\pi/2$, $\theta_B = 84.4$ deg, while $\psi_n = 35.3$ deg. The relative Darwin width amount to about $2 \cdot 10^{-6}$, with a very high transmissivity (about 97%). Our calculations show that one can reach pulse power in excess of 600 GW at 12 keV with a FWHM relative bandwidth of about $5 \cdot 10^{-5}$.

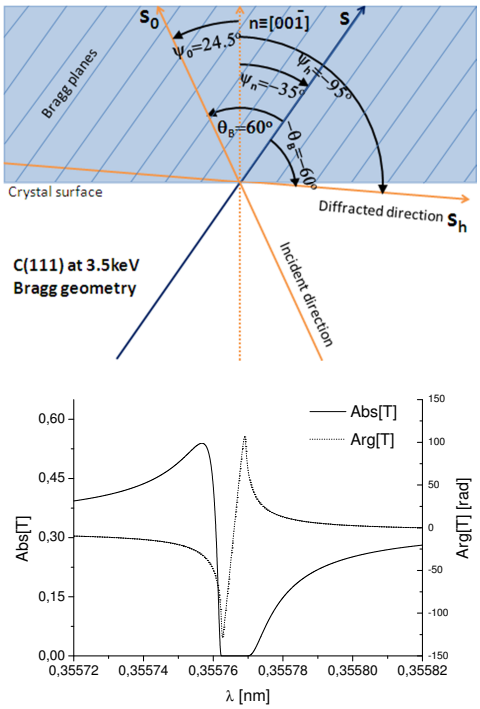

Fig. 3. Scattering geometry, modulus and phase of the transmittance for the C(111) asymmetric Bragg reflection from the 100 μm thick perfect diamond crystal in Fig. 2 at 3.5 keV.

For self-seeding implementation, we are interested in the forward diffracted, i.e. in the transmitted beam for each of these reflections. From this viewpoint, the crystal can be characterized as a filter with given complex transmissivity. We will now consider the three transmissivity separately, showing their amplitude and phase, together with the crystal geometry for fixed energy points.

In Fig. 3 we show the amplitude and the phase for the C(111) asymmetric Bragg reflection at 3.5 keV. The following Fig. 4 shows the same reflection at a higher energy, 5 keV. In this case, one has Laue geometry. In Fig. 5 we plot the same quantities for the C(113) asymmetric Bragg geometry at 7 keV. In Fig. 6 we consider the symmetric Bragg reflection C(004) at 8 keV and, finally, in Fig. 7 we plot amplitude and phase for the asymmetric Bragg reflection C(333) at 9 keV. By inspecting the plots, the reader can easily see the difference between Bragg and Laue geometry, as well as that between symmetric and asymmetric reflections.

Amplitude and phase in the plots are related by Kramers-Kroning relations. Let us regard our crystal as a filter with transmission $T(\omega) = |T(\omega)| \exp[i\Phi(\omega)]$. According to Titchmarsch theorem (see [24] and refer-

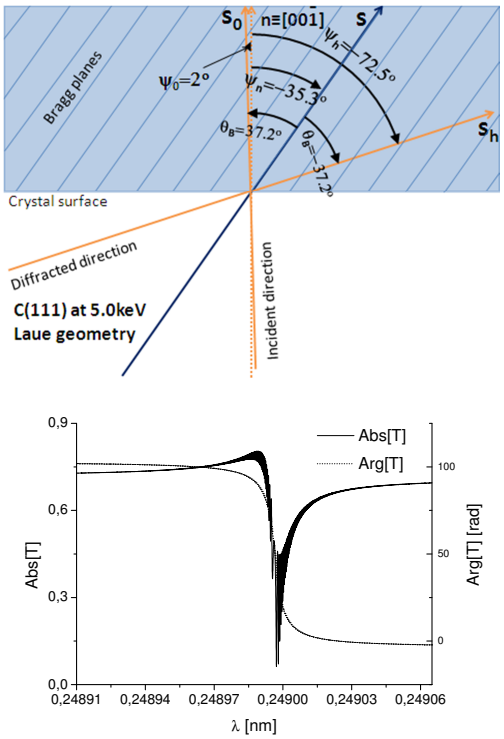

Fig. 4. Scattering geometry, modulus and phase of the transmittance for the asymmetric C(111) Laue reflection from the 100 μm thick perfect diamond crystal in Fig. 2 at 5 keV.

ences therein for a recent review on the subject) causality [3] and square-integrability of the inverse Fourier transform of $T(\omega) = |T(\omega)| \exp[i\Phi(\omega)]$, which will be indicated with $\mathcal{T}(t)$, is equivalent [4] to the existence of an analytic continuation of $T(\omega)$ to $\Omega = \omega + i\omega'$ on the upper complex Ω-plane (i.e. for $\omega' > 0$). The same theorem also shows that the two previous statements are equivalent to the fact that real and imaginary part of $T(\omega)$ are connected by Hilbert transformation. Since $\mathcal{T}(t)$ must be real (thus implying that $T^*(\omega) = T(-\omega)$), from the Hilbert transformation follows the well-known Kramers-Kroninig relations [25, 26], linking real and imaginary part of $T(\omega)$.

A similar reasoning can be done for the modulus $|T(\omega)|$ and the phase $\Phi(\omega)$, see [27]. In fact, one can write

$$\ln[T(\omega)] = \ln[|T(\omega)|] + i\Phi(\omega)\,, \tag{11}$$

[3] Causality simply requires that the filter can respond to a physical input after the time of that input and never before.

[4] Here we are tacitly assuming, as required by Titchmarsh theorem, that $T(\omega)$ is a square integrable function.

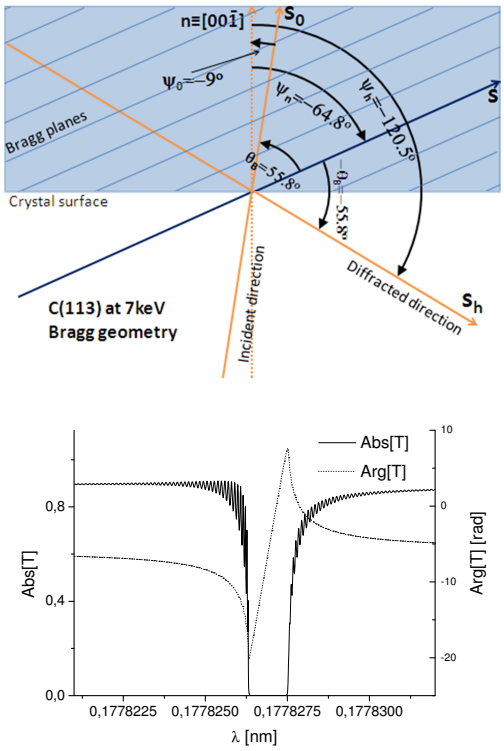

Fig. 5. Scattering geometry, modulus and phase of the transmittance for the asymmetric C(113) Bragg reflection from the 100 μm thick perfect diamond crystal in Fig. 2 at 7 keV.

that play a similar role to real and imaginary part of the refractive index of a given medium.

Note that $T^*(\omega) = T(-\omega)$ implies that $|T(\omega)| = |T(-\omega)|$ and that $\Phi(\omega) = -\Phi(-\omega)$. Therefore, using Eq. (11) one also has that $\ln[T(\omega)]^* = \ln[T(-\omega)]$. Application of Titchmarsh theorem shows that the analyticity of $\ln[|T(\Omega)|]$ on the upper complex Ω-plane implies that $\Phi(\omega)$ can be obtained from $|T(\omega)|$. As is well known however, in applying such procedure one tacitly assumes that $\ln[T(\Omega)]$ is analytical on the upper complex Ω-plane. While causality implies this fact for $T(\Omega)$, it does not imply it automatically for $\ln[|T(\Omega)|]$. In fact, such function is singular where $T(\Omega) = 0$. If $T(\Omega)$ has zeros on the upper complex plane, these zeros would contribute adding extra terms to the total phase. It can be shown that $T(\Omega)$ does not have zeros on the upper complex plane, and that Titchmarsch theorem actually applies.

The simplest check of the correctness of the calculations by means of dynamical theory consists, therefore, in verifying that amplitude and phase of the transmissivity are actually related by Kramers-Kroning relations.

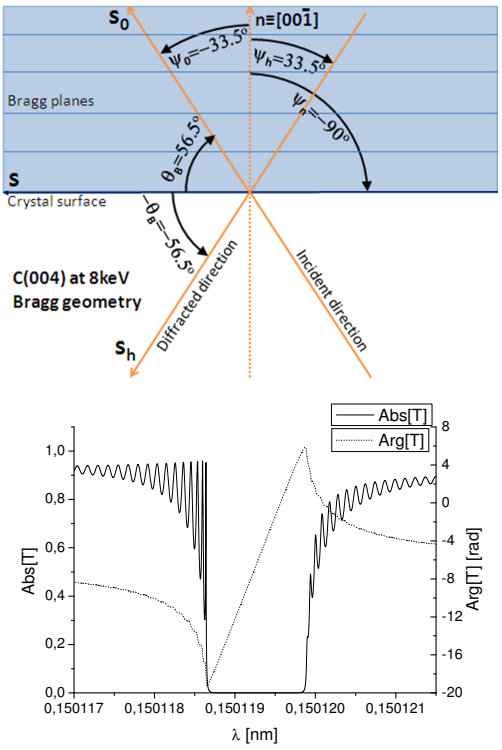

Fig. 6. Scattering geometry, modulus and phase of the transmittance for the symmetric C(004) Bragg reflection from the 100 μm thick perfect diamond crystal in Fig. 2 at 8 keV.

3 Spatiotemporal shift and its influence on input coupling factor

A wake monochromator introduces spatiotemporal deformations of the seeded X-ray pulse, which can be problematic for seeding. The spatiotemporal coupling in the electric field relevant to self-seeding schemes with crystal monochromators has been analyzed in the framework of classical dynamical theory of X-ray diffraction [23].

This analysis shows that a crystal in Bragg or Laue geometry transforms the incident electric field $E(x,t)$ in the $\{x,t\}$ domain into $E(x-at,t)$, where a = const. The physical meaning of this distortion is that the beam spot size is independent of time, but the beam central position changes as the pulse evolves in time. First we will show in a simple manner that, based on the only use of the Bragg law, we can directly arrive to an explanation of spatiotemporal coupling phenomena in the dynamical theory of diffraction [28].

The transmissivity curve - the transmittance - in asymmetric and symmetric Bragg or Laue geometry can be expressed in the framework of dynamical

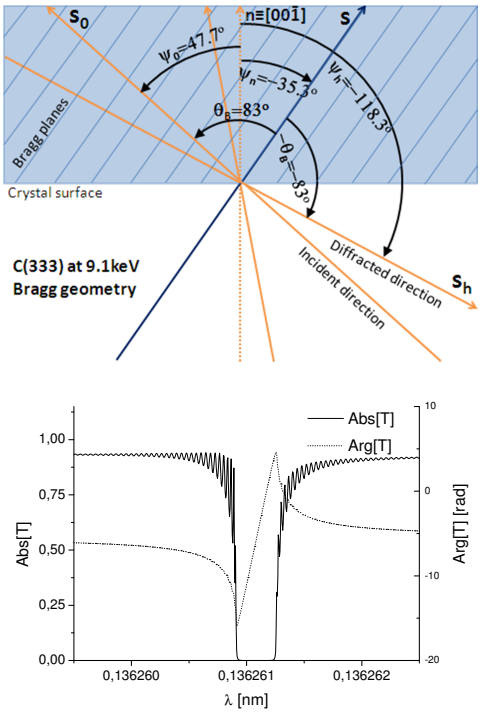

Fig. 7. Scattering geometry, modulus and phase of the transmittance for the asymmetric C(333) Bragg reflection from the 100 μm thick perfect diamond crystal in Fig. 2 at 9 keV.

theory with the help of Eq. (5). Transmitted (i.e. forward diffracted) beam and incident beam have the same direction. Therefore we set $\theta_i = \theta_d$. Using the symbol T for transmittance, Eq. (5) yields

$$T(\Delta\omega, \Delta\theta_i) = T(\Delta\omega + \omega_B \Delta\theta \cot(\theta_B)) \,, \tag{12}$$

where $\Delta\omega = (\omega - \omega_B)$ and $\Delta\theta = (\theta_i - \theta_B)$ are the deviations of frequency and incident angle of the incoming beam from Bragg frequency and Bragg angle respectively. The frequency ω_B and the angle θ_B are obviously related by the Bragg law: $\omega_B \sin(\theta_B) = \pi c/d$.

It should be realized that the crystal does not introduce an angular dispersion similar to the grating. However, a more detailed analysis based on the expression for the transmissivity, Eq. (12), shows that a less well-known spatiotemporal coupling exists. Let us discuss this fact. It is evident by inspection of Eq. (12), that the transmissivity is invariant under angle and frequency transformations obeying

$$\Delta\omega + \omega_B \Delta\theta \cot(\theta_B) = \text{const} \,. \tag{13}$$

This corresponds to the coupling in the Fourier domain. In general, one

would indeed expect the transformation to be symmetric in both the Fourier domain $\{k_x, \omega\}$ (with $k_x = \omega_B \Delta\theta/c$) and in the space-time domain $\{x, t\}$, due to the symmetry of the transfer function. However, it is reasonable to expect the influence of a nonsymmetric input beam distribution. The field transformation for the XFEL pulse after the crystal in the $\{x, t\}$ domain is given by

$$E_{\text{out}}(x,t) = FT\{T[\Delta\omega, (k_x)_{\text{in}}, (k_x)_{\text{out}}]E_{\text{in}}(\Delta\omega, k_x)\}\ , \tag{14}$$

where FT indicates a Fourier transform from the frequency domain $\{k_x, \omega\}$ to the space-time domain $\{x, t\}$.

In the self-seeding case, the incoming XFEL beam is well collimated, meaning that its angular spread is a few times smaller than the angular width of the transfer function. Yet, the spectral bandwidth of the incoming beam is much wider than the bandwidth of the transfer function. Under the limit of a wide spectral bandwidth for the incoming beam (with respect to the bandwidth of the transfer function), and applying the shift theorem twice we obtain

$$\begin{aligned} E_{\text{out}}(x,t) &= \eta(t) \int dk_x \exp(i \cot\theta_B k_x c t) \exp(-i k_x x) E(\omega_B, k_x) \\ &= \eta(t) a(x - c\cot\theta_B t)\ , \end{aligned} \tag{15}$$

where

$$\eta(t) = \frac{1}{2\pi} \int d\omega \exp(-i\omega t) T(\omega) \tag{16}$$

is the inverse temporal Fourier transform of the transmittance curve (impulse response). Eq. (15) is universal i.e. valid for both symmetric and asymmetric Bragg and Laue geometries.

The spatial shift given by Eq. (15) is proportional to $\cot(\theta_B)$, and is maximal in the range for small values of θ_B. Therefore, the spatiotemporal coupling is an issue, and efforts are necessarily required to avoid distortions. A geometry with θ_B close to $\pi/2$ would be a more advantageous option from this view point, albeit with decrease in the spectral tunability [23].

3.1 Influence of the offset on the coupling factor

The influence of the spatiotemporal distortion on the operation of the self-seeding setup can be quantified by studying the input coupling factor be-

tween the seed beam and the ground eigenmode of the FEL amplifier. When the undulator is sufficiently long, the output energy in the FEL pulse grows exponentially with the undulator length, and the eenrgy gain, $G = E_{\rm out}/E_{\rm ext}$, can be written as

$$G = A \exp[z/L_g] \,, \tag{17}$$

where A is the input coupling factor. In the linear regime the energy gain does not depend on the input energy $E_{\rm ext}$, and for the case including spatial shift the input coupling factor A allows for a simple and convenient measure of the departure from the ideal situation. In our case this measure is simply defined as

$$Q \equiv \frac{E_{\rm nonideal}}{E_{\rm ideal}} = \frac{A_{\rm nonideal}}{A_{\rm ideal}} \,. \tag{18}$$

We will consider a particular example for $\lambda = 0.15$ nm, corresponding to about 8 keV. We simulated the SASE process in the first 11 cells, followed by the self-seeding setup exploiting the C(004) reflection. The seed beam is then superimposed again onto the electron bunch (the modulation having been washed out by the chicane). We calculate the output power and spectrum after 6 cells, which is still in the linear regime, and we scan over the transverse offset.

A few examples of the output obtained with this procedure are shown in Fig. 8, which compares the result for zero offset (black solid lines) with those for 2 μm, 18 μm, and 34 μm (red dotted lines). All results refer to a single simulation shot. The plots on the left show the transverse profile of the photon beam after 6 undulator cells following the self-seeding setup. The figures in the middle show the power, and those on the left the spectra. Qualitatively, the effect due to the transverse offset is easy to see by inspection.

The energy as a function of the position into the radiator is shown in Fig. 9. The function $Q(\Delta)$ instead, is shown in Fig. 10. Note that the input coupling factor does not drop abruptly to zero when Δ is of order of the rms transverse size of the photon beam. This is because the photon beam intensity does not drop off as a Gaussian function. As a result, on can qualitatively go to larger deviations of θ_B, still obtaining a reasonable coupling factor.

We hope that these considerations will be useful for FEL physicists in the design stage of wake monochromator setups.

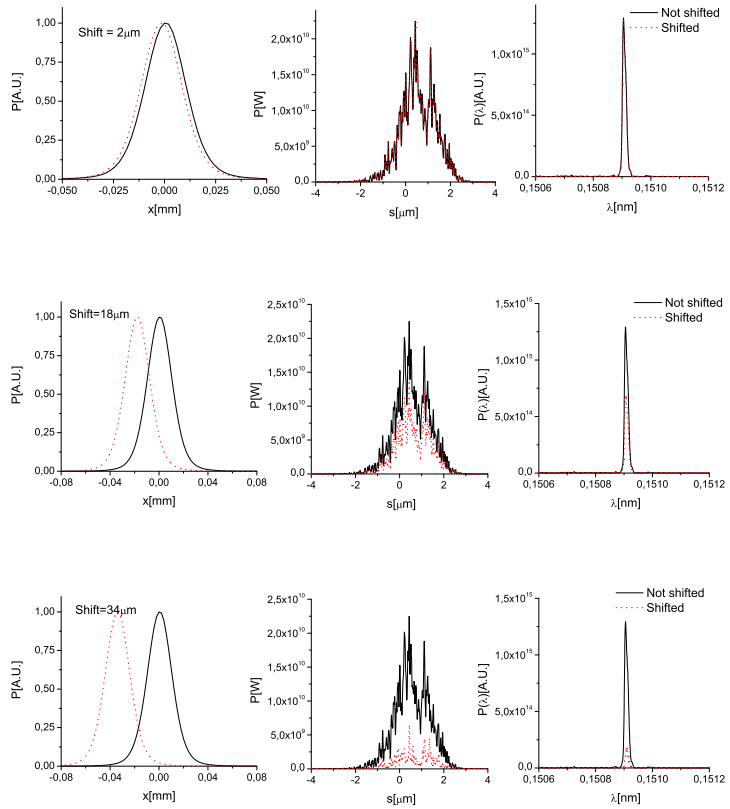

Fig. 8. Comparison between the self-seeded output with (red, dotted lines) and without (black, solid lines) transverse offset, at different offset values. The left plots show the photon beam transverse profiles, the middle plots show the power, the right plots show the spectra. All plots refer to a single simulation shot.

4 FEL studies

In order to quantitatively investigate the effects of the spatial shift on the FEL amplification process, we performed numerical simulations using the code Genesis [29]. Simulations are based on a statistical analysis consisting of 100 runs. We consider the setup in Fig. 11, with reference to [7] for details. In this article we are interested in the energy range where hard X-ray self seeding can be implemented, starting from 3.5 keV up to 13 keV. The C(111) reflections (Bragg and Laue) will be used in the second chicane. C(113), C(004) and C(333) reflections will be used in the third chicane. Since we are interested in energies starting from 3.5 keV, we fix the electron energy at 17.5 GeV. The lower energy is used in the very soft X-ray regime, see [7], between 0.3 keV and 0.5 keV, which is outside the interests of this article, and where one relies on a grating monochromator. In Fig. 12 we plot the results of start-to-end simulations [30], while the main undulator parameters are reported in Table 2. Our simulations automatically include the influence of

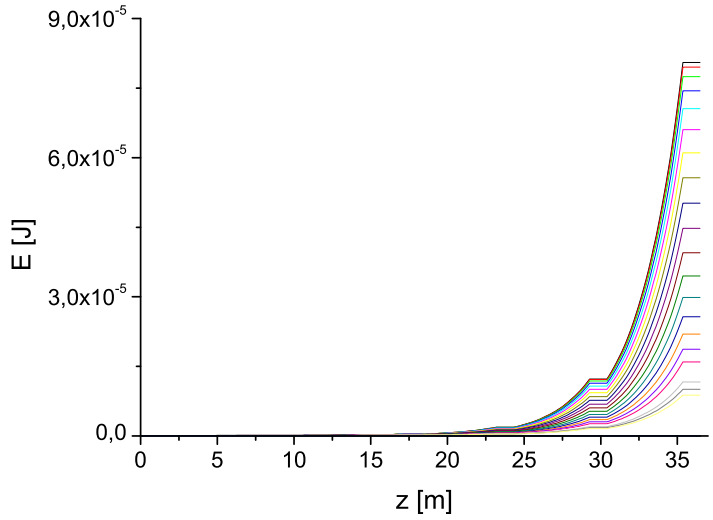

Fig. 9. Collected energies as a function of the position inside the radiator, for increasing offset from 0 μm to 40 μm with steps of 2 μm.

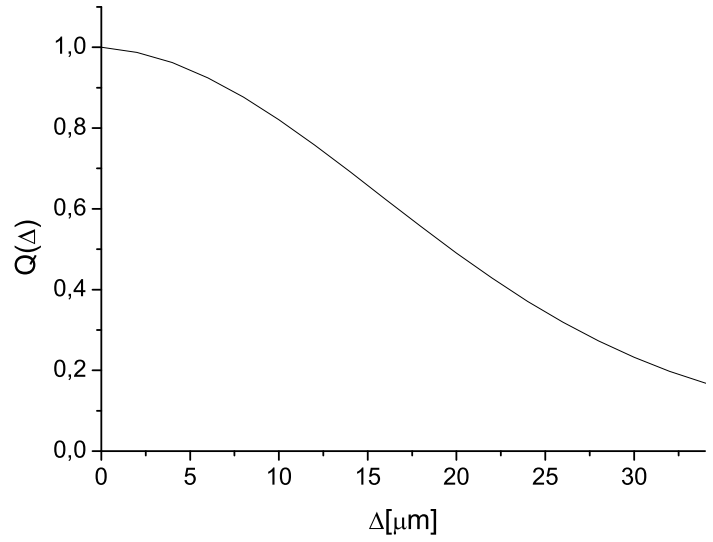

Fig. 10. Measure of the dependence of the input coupling factor on the offset $Q(\Delta)$.

the spatial shift of the photon beam induced by the crystal. We will present results for the different reflections at given energy points.

As is explained in detail in [7], in the range between 3 keV and 5 keV the first chicane is not used and is switched off. After the first 7 cells the electron and the photon beams are separated with the help of the second magnetic chicane, and the C(111) reflection is used to monochromatize the radiation. The seed is amplified in the next 4 cells. After that, the electron and the

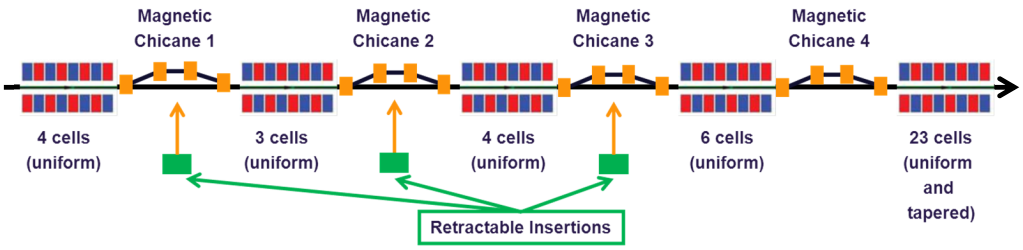

Fig. 11. Schematic setup of the bio-imaging beamline discussed in [7].

Table 2
Undulator parameters

	Units	
Undulator period	mm	68
Periods per cell	-	73
Total number of cells	-	40
Intersection length	m	1.1
Photon energy	keV	0.3-13

photon beam are separated again by the third chicane, and an X-ray optical delay line allows for the introduction of a tunable delay of the photon beam with respect to the electron beam. The following 6 cells use only a part of the electron beam as a lasing medium. A magnetic chicane follows, which shifts the unspoiled part of the electron bunch on top of the of the photon beam. In this way, a fresh bunch technique can be implemented. Since the delays are tunable, the photon pulse length can be tuned. Finally, radiation is amplified into the last 23 tapered cells to provide pulses with about 2 TW power.

In partial difference with respect to what has been discussed in [7], for energies lower than 5 keV we used the asymmetric C(111) reflection (Bragg and Laue geometry), while in [7] we exploited the C(111) symmetric Bragg reflection only. Moreover, for energies larger than 5 keV we rely on a crystal placed after 11 cells, and we take advantage of the C(113), the C(004) and the C(333) reflections. In this case the fourth chicane is switched off. If tunability of the pulse duration is requested in this energy range, this is most easily achieved by providing additional delay with the fourth magnetic chicane installed behind the hard X-ray self-seeding setup.

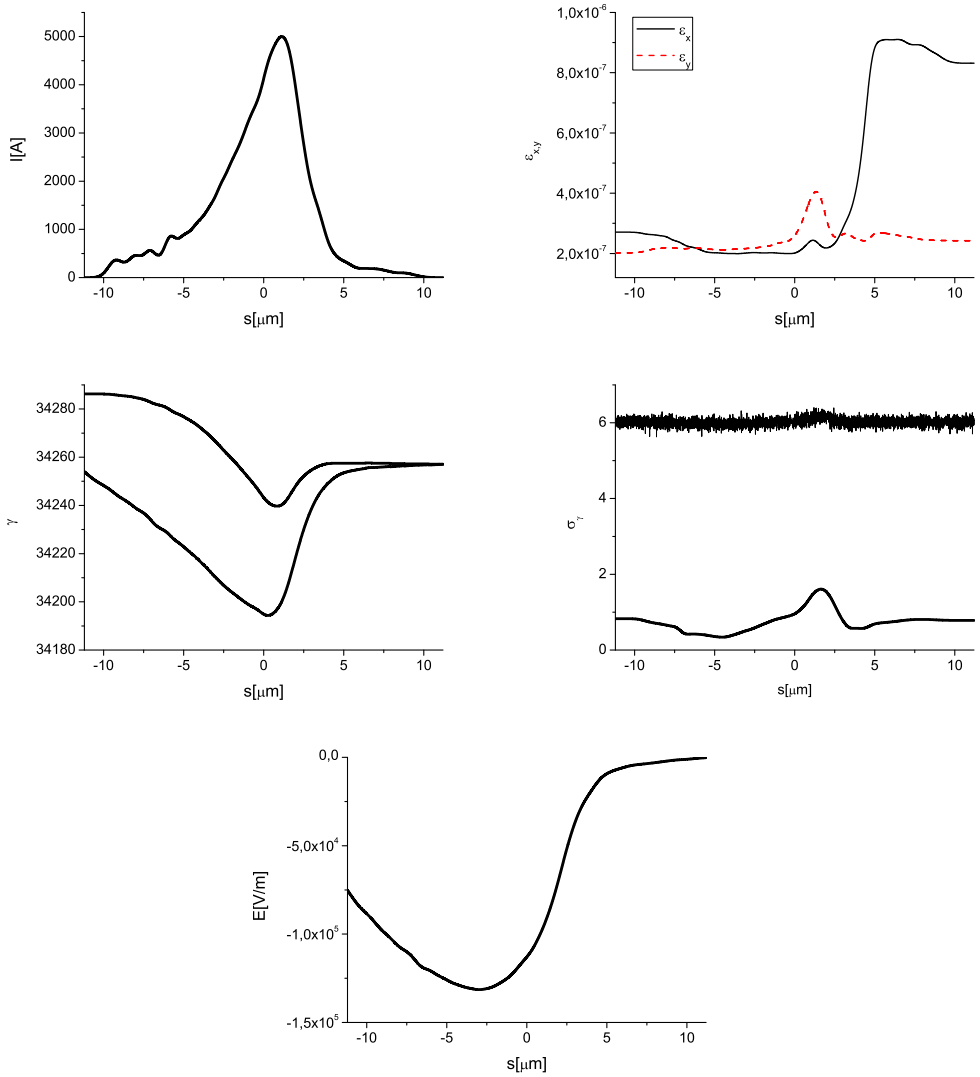

Fig. 12. Results from electron beam start-to-end simulations at the entrance of the undulator system of the bio-imaging beamline [30] for the hard X-ray case for the 17.5 GeV mode of operation. (First Row, Left) Current profile. (First Row, Right) Normalized emittance as a function of the position inside the electron beam. (Second Row, Left) Energy profile along the beam, lower curve. The effects of resistive wakefields along SASE1 are illustrated by the comparison with the upper curve, referring to the entrance of SASE1 (Second Row, Right) Electron beam energy spread profile, upper curve. The effects of quantum diffusion along SASE1 are illustrated by the comparison with the lower curve, referring to the entrance of SASE1. (Bottom row) Resistive wakefields in the SASE3 undulator [30].

4.1 C(111) asymmetric Bragg reflection at 3.5 keV

As discussed above, the first chicane is switched off, so that the first part of the undulator effectively consists of 7 uniform cells. We begin our investiga-

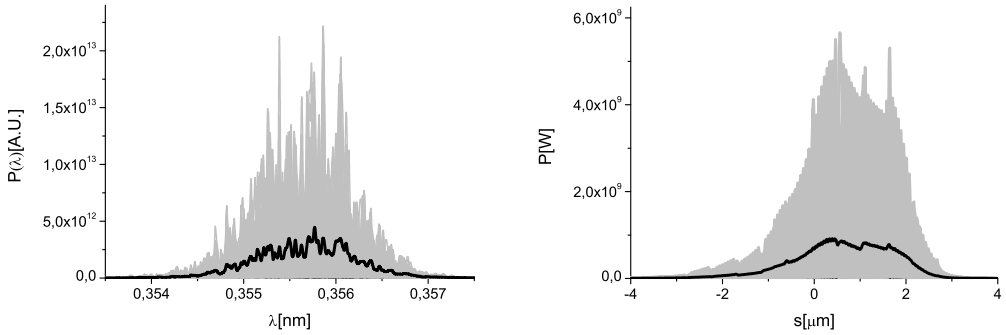

Fig. 13. Power and spectrum at 3.5 keV before the second magnetic chicane. Grey lines refer to single shot realizations, the black line refers to the average over a hundred realizations.

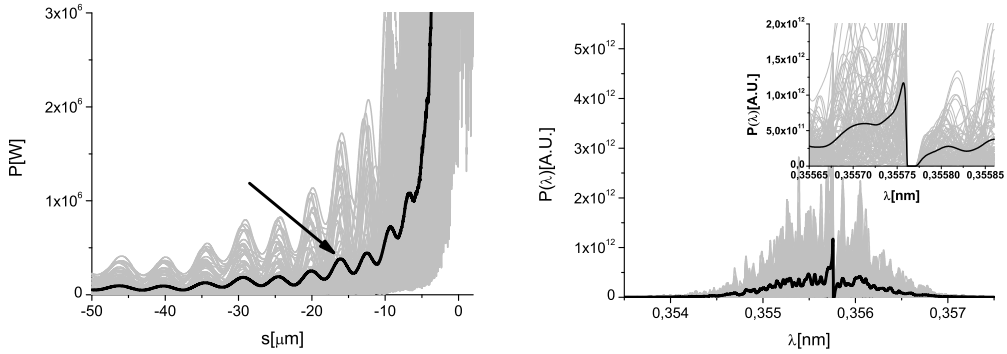

Fig. 14. Power and spectrum at 3.5 keV after the single crystal self-seeding X-ray monochromator. A 100 μm thick diamond crystal (C(111) Bragg reflection, σ-polarization) is used. Grey lines refer to single shot realizations, the black line refers to the average over a hundred realizations. The black arrow indicates the seeding region.

tion by simulating the SASE power and spectrum after the first part of the undulator, that is before the second magnetic chicane in the setup. Results are shown in Fig. 13.

The second magnetic chicane is switched on, and the single-crystal X-ray monochromator is set into the photon beam. We take advantage of the C(111) Bragg reflection, σ-polarization, Fig. 14. As discussed before, the modulus and the phase of the crystal transmissivity are related by Kramers-Kroening relations. The numerical accuracy with which causality is satisfied in our simulations can be shown by a logarithmic plot of the FEL pulse power after the crystal, Fig. 15. The peak in the center is the main FEL pulse. On the left side one can identify the seed pulse. The large jump between the power after transmission (on the right side of the peak in the center) is due to causality, and is strictly connected with the fact that the phase in the transmission

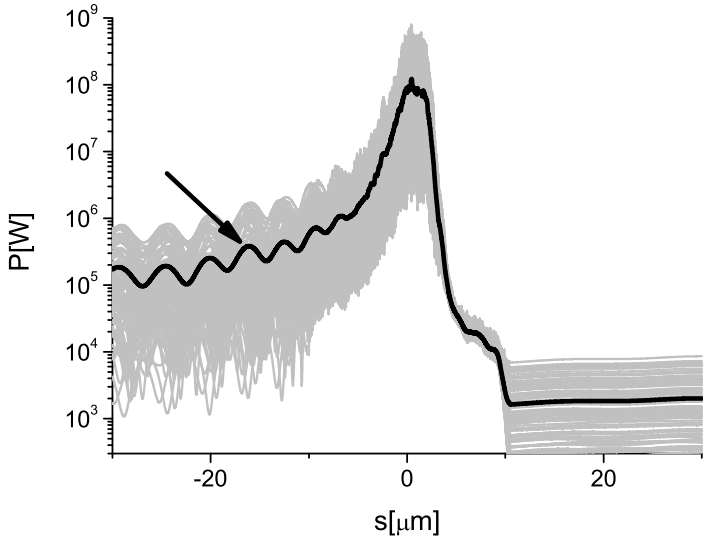

Fig. 15. Logarithmic plot of the power at 3.5 keV after the single crystal self-seeding X-ray monochromator. The black arrow indicates the seeding region. The region on the right hand side of the plot (before the FEL pulse) is nominally zero because of causality reasons. Differences with respect to zero give back the accuracy of our calculations.

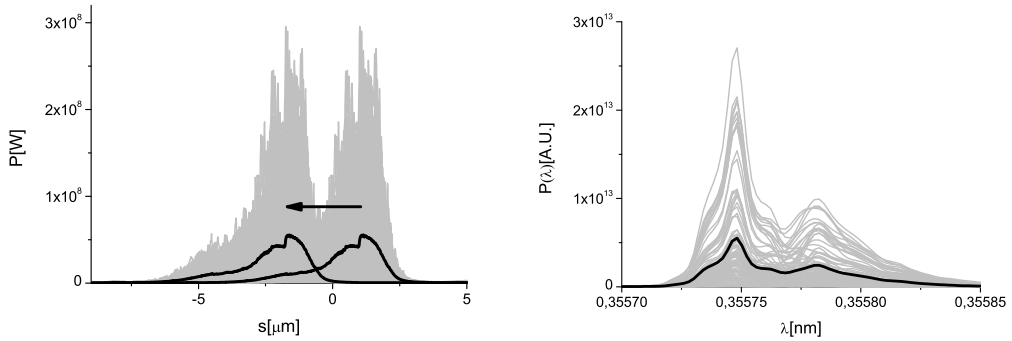

Fig. 16. Power and spectrum at 3.5 keV after the third chicane equipped with the X-ray optical delay line, delaying the radiation pulse with respect to the electron bunch. Grey lines refer to single shot realizations, the black line refers to the average over a hundred realizations.

function is properly accounted for. For example, if a transmission without phase were used, one would have obtained a symmetric behavior, which is not causal at all. The small ($\sim 10^{-3}$) but visible departure from the exact zero appearing in the right-hand side of Fig. 15 is related with the accuracy of our calculations. This accuracy is acceptable for most purposes.

Following the seeding setup, the electron bunch amplifies the seed in the following 4 undulator cells. After that, a third chicane is used to allow for

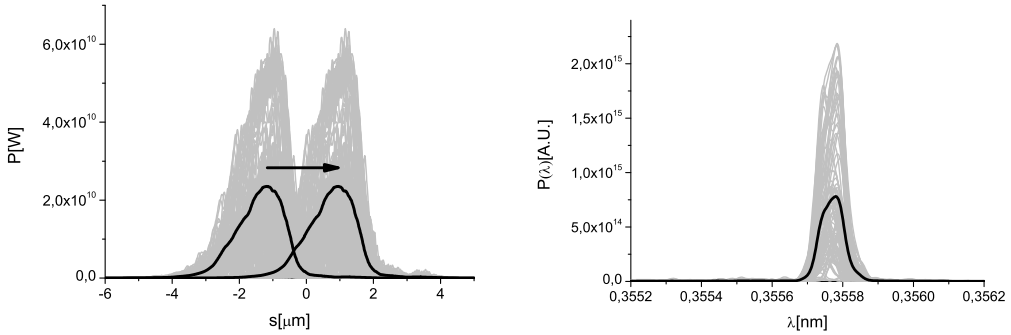

Fig. 17. Power and spectrum at 3.5 keV after the last magnetic chicane. Grey lines refer to single shot realizations, the black line refers to the average over a hundred realizations.

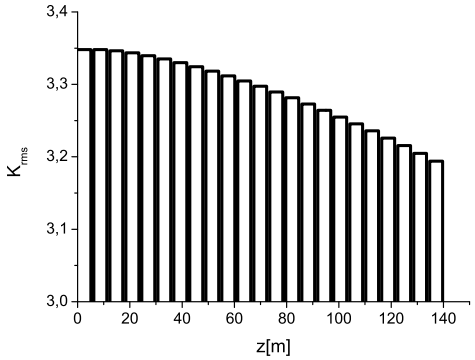

Fig. 18. Tapering law at 3.5 keV.

the installation of an x-ray optical delay line, which delays the radiation pulse with respect to the electron bunch. The power and spectrum of the radiation pulse after the optical delay line are shown in Fig. 16, where the effect of the optical delay is illustrated.

Due to the presence of the optical delay, only part of the electron beam is used to further amplify the radiation pulse in the following 6 undulator cells. The electron beam part which is not exploited is fresh, and can further lase. In order to allow for that, after amplification, the electron beam passes through the final magnetic chicane, which delays the electron beam. The power and spectrum of the radiation pulse after the last magnetic chicane are shown in Fig. 17. By delaying the electron bunch, the magnetic chicane effectively shifts forward the photon beam with respect to the electron beam. Tunability of such shift allows the selection of different photon pulse length.

The last part of the undulator is composed by 23 cells. It is partly tapered post-saturation, to increase the region where electrons and radiation interact properly to the advantage of the radiation pulse. Tapering is implemented by

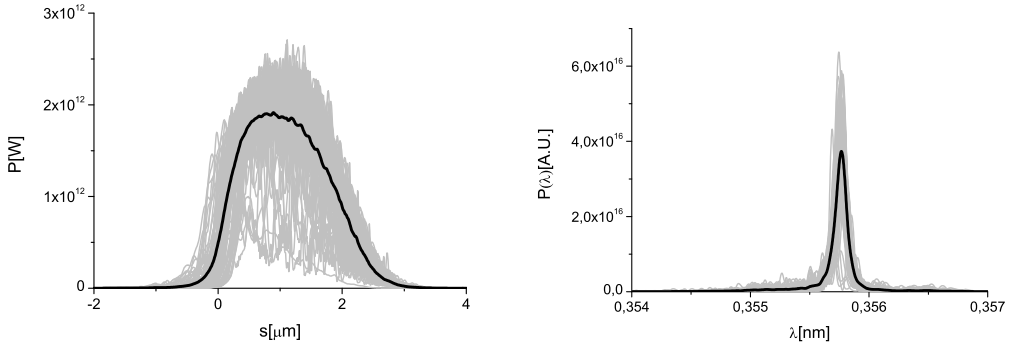

Fig. 19. Final output. Power and spectrum after tapering at 3.5 keV. Grey lines refer to single shot realizations, the black line refers to the average over a hundred realizations.

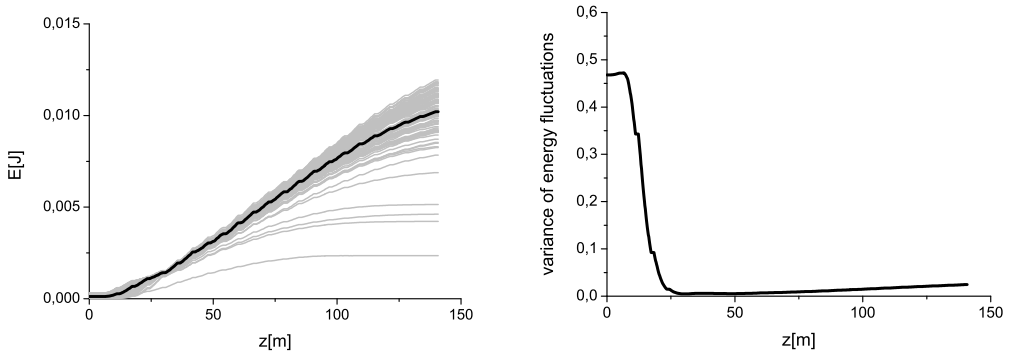

Fig. 20. Final output. Energy and energy variance of output pulses at 3.5 keV. In the left plot, grey lines refer to single shot realizations, the black line refers to the average over a hundred realizations.

changing the K parameter of the undulator segment by segment according to Fig. 18. The tapering law used in this work has been implemented on an empirical basis.

The use of tapering together with monochromatic radiation is particularly effective, since the electron beam does not experience brisk changes of the ponderomotive potential during the slippage process. The final output is presented in Fig. 19 in terms of power and spectrum. As one can see, simulations indicate an output power of about 2 TW.

The energy of the radiation pulse and the energy variance are shown in Fig. 20 as a function of the position along the undulator. The divergence and the size of the radiation pulse at the exit of the final undulator are shown, instead, in Fig. 21. In order to calculate the size, an average of the transverse intensity profiles is taken. In order to calculate the divergence, the spatial Fourier transform of the field is calculated.

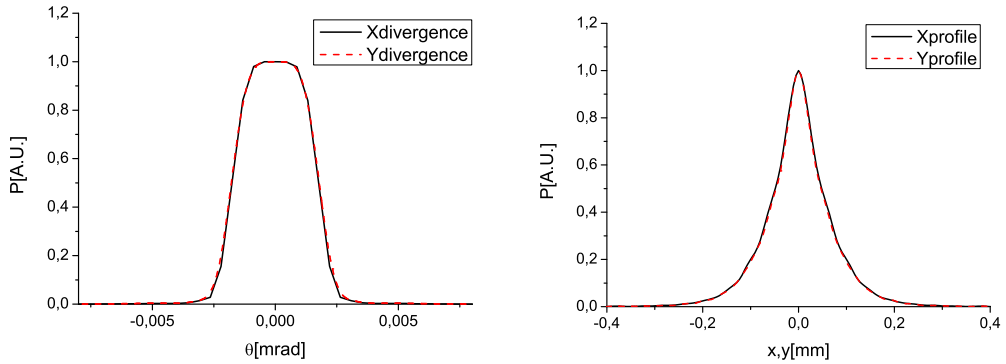

Fig. 21. Final output. X-ray radiation pulse energy distribution per unit surface and angular distribution of the X-ray pulse energy at 3.5 keV at the exit of output undulator.

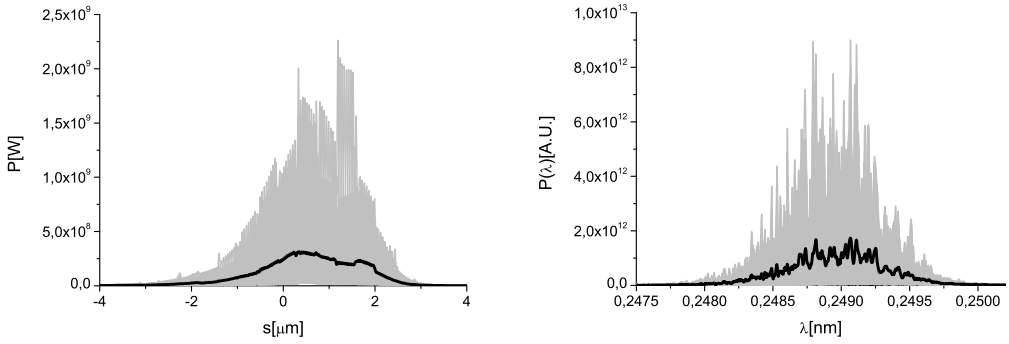

Fig. 22. Power and spectrum at 5 keV before the second magnetic chicane. Grey lines refer to single shot realizations, the black line refers to the average over a hundred realizations.

4.2 C(111) asymmetric Laue reflection at 5.0 *keV*

Operation at 5 keV is identical to the case for 3.5 keV. The only difference is that now the Laue C(111) reflection is used.

As before, the first chicane is switched off, so that the first part of the undulator effectively consists of 7 uniform cells. After the first part of the undulator, one has the power and spectrum shown in Fig. 22. The second magnetic chicane is switched on, and the single-crystal X-ray monochromator is set into the photon beam. We take advantage of the C(111) Laue reflection, σ-polarization, Fig. 23.

Exactly as before, following the seeding setup, the electron bunch amplifies the seed in the following 4 undulator cells. After that, a third chicane is used to allow for the installation of an x-ray optical delay line, which delays the

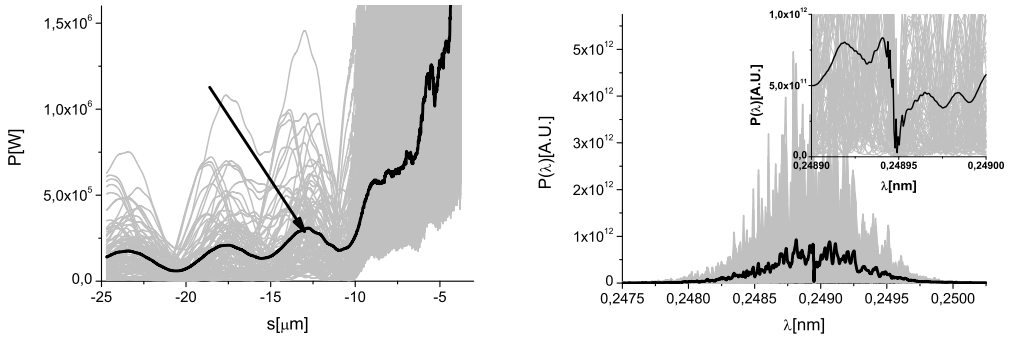

Fig. 23. Power and spectrum at 5 keV after the single crystal self-seeding X-ray monochromator. A 100 μm thick diamond crystal (C(111) Laue reflection, σ-polarization) is used. Grey lines refer to single shot realizations, the black line refers to the average over a hundred realizations. The black arrow indicates the seeding region.

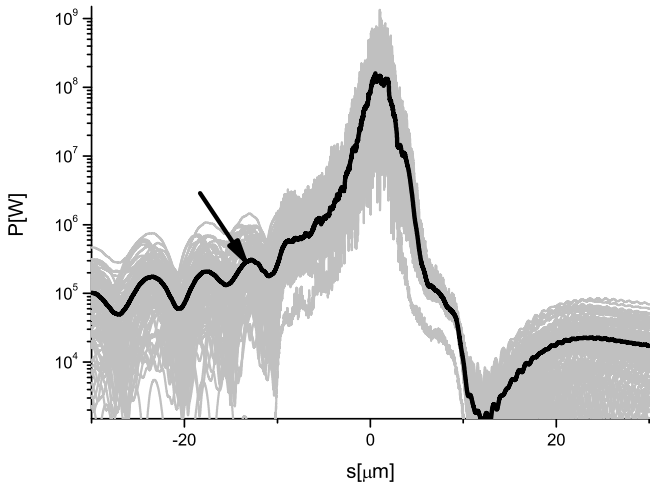

Fig. 24. Logarithmic plot of the power at 5 keV after the single crystal self-seeding X-ray monochromator. The black arrow indicates the seeding region. The region on the right hand side of the plot (before the FEL pulse) is nominally zero because of causality reasons. Differences with respect to zero give back the accuracy of our calculations.

radiation pulse with respect to the electron bunch. The power and spectrum of the radiation pulse after the optical delay line are shown in Fig. 25, where the effect of the optical delay is illustrated. The numerical accuracy with which causality is satisfied in our simulations can be shown by a logarithmic plot of the FEL pulse power after the crystal, Fig. 24. The peak in the center is the main FEL pulse. On the left side one can identify the seed pulse. One

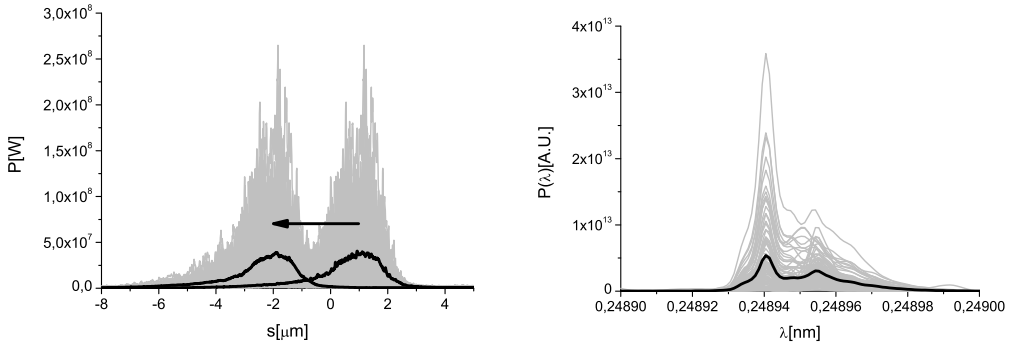

Fig. 25. Power and spectrum at 5 keV after the third chicane equipped with the X-ray optical delay line, delaying the radiation pulse with respect to the electron bunch. Grey lines refer to single shot realizations, the black line refers to the average over a hundred realizations.

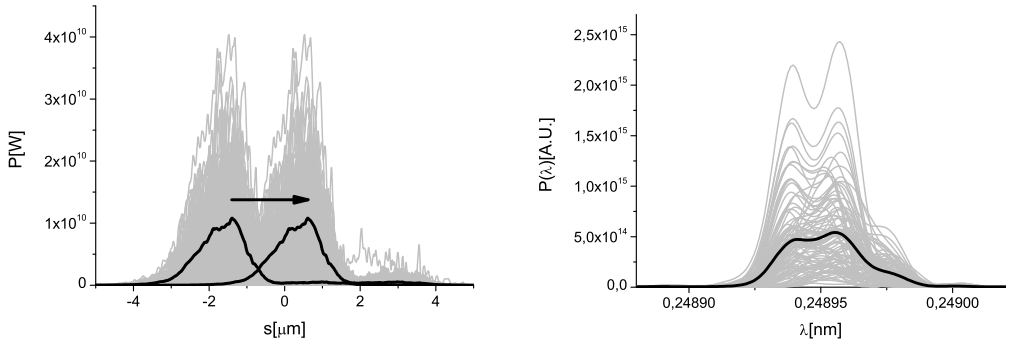

Fig. 26. Power and spectrum at 5 keV after the last magnetic chicane. Grey lines refer to single shot realizations, the black line refers to the average over a hundred realizations.

the right side, before the FEL pulse, one has nominally zero power.

Due to the presence of the optical delay, only part of the electron beam is used to further amplify the radiation pulse in the following 6 undulator cells. The electron beam part which is not used is fresh, and can be used for further lasing. In order to do so, after amplification, the electron beam passes through the final magnetic chicane, which delays the electron beam. The power and spectrum of the radiation pulse after the last magnetic chicane are shown in Fig. 26. By delaying the electron bunch, the magnetic chicane effectively shifts forward the photon beam with respect to the electron beam. Tunability of such shift allows the selection of different photon pulse length.

The last part of the undulator is composed by 23 cells. It is partly tapered post-saturation, to increase the region where electrons and radiation interact properly to the advantage of the radiation pulse. Tapering is implemented by changing the K parameter of the undulator segment by segment according

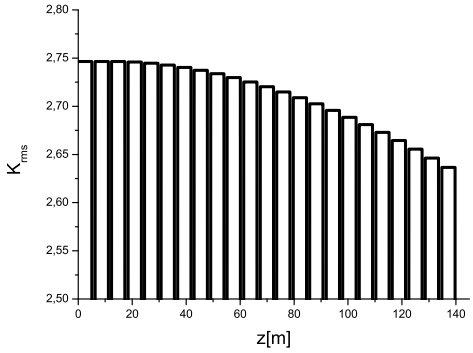

Fig. 27. Tapering law at 5 keV.

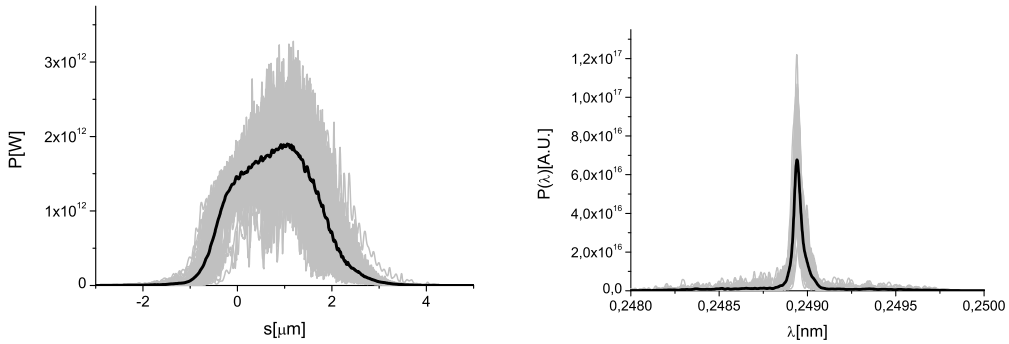

Fig. 28. Final output. Power and spectrum after tapering at 5 keV. Grey lines refer to single shot realizations, the black line refers to the average over a hundred realizations.

to Fig. 27. The tapering law used in this work has been implemented on an empirical basis.

As explained before, the use of tapering together with monochromatic radiation is particularly effective. The final output is presented in Fig. 28 in terms of power and spectrum. As one can see, simulations indicate an output power of about 2 TW.

The energy of the radiation pulse and the energy variance are shown in Fig. 29 as a function of the position along the undulator. The divergence and the size of the radiation pulse at the exit of the final undulator are shown, instead, in Fig. 30.

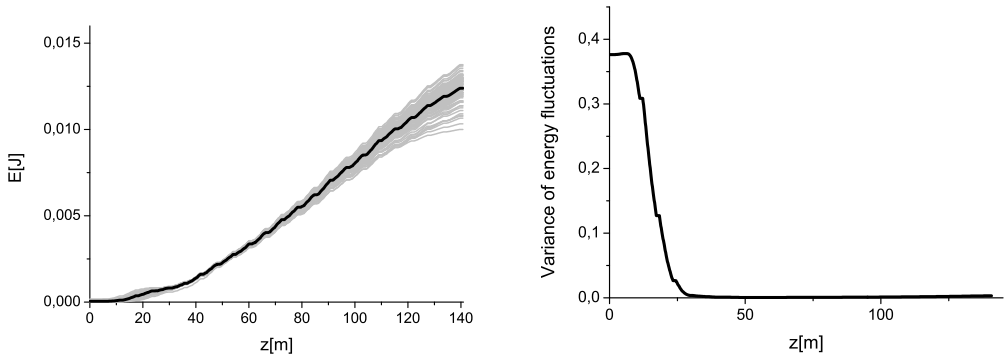

Fig. 29. Final output. Energy and energy variance of output pulses at 5 keV. In the left plot, grey lines refer to single shot realizations, the black line refers to the average over a hundred realizations.

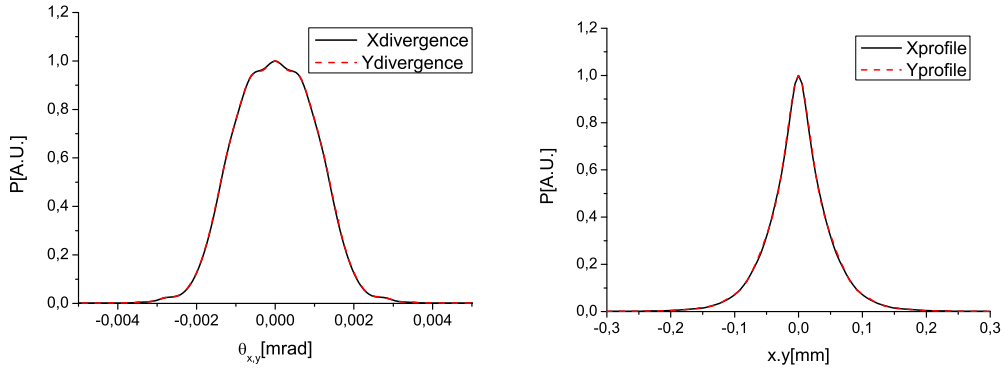

Fig. 30. Final output. X-ray radiation pulse energy distribution per unit surface and angular distribution of the X-ray pulse energy at 5 keV at the exit of output undulator.

4.3 C(113) asymmetric Bragg reflection at 7 keV

We now consider the energy point at 7 keV. In this case a simpler scheme with a single hard x-ray self-seeding setup is considered. The first two magnetic chicanes are switched off. Therefore, the electron beam lases in SASE mode along the first 11 undulator cells before passing through the single-crystal monochromator filter. The input power and spectrum are shown in Fig. 31.

The effect of the filtering process is illustrated, both in the time and in the frequency domain, in Fig. 32.

The numerical accuracy with which causality is satisfied in our simulations can be shown by a logarithmic plot of the FEL pulse power after the crystal, Fig. 33. The peak in the center is the main FEL pulse. On the left side one

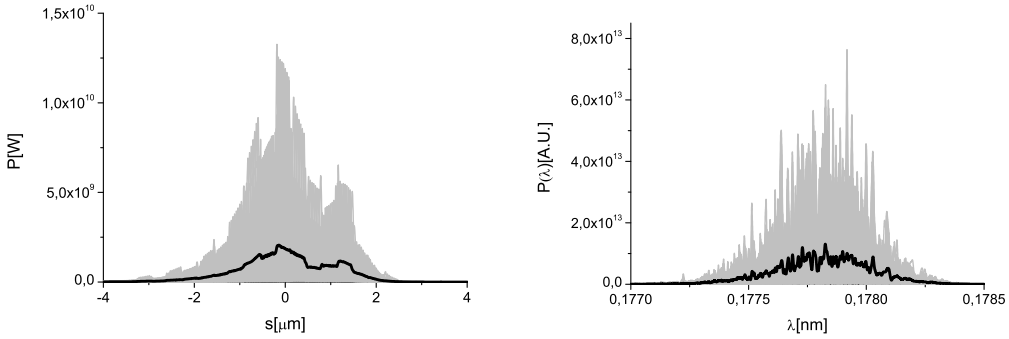

Fig. 31. Power and spectrum at 7 keV before the third magnetic chicane. Grey lines refer to single shot realizations, the black line refers to the average over a hundred realizations.

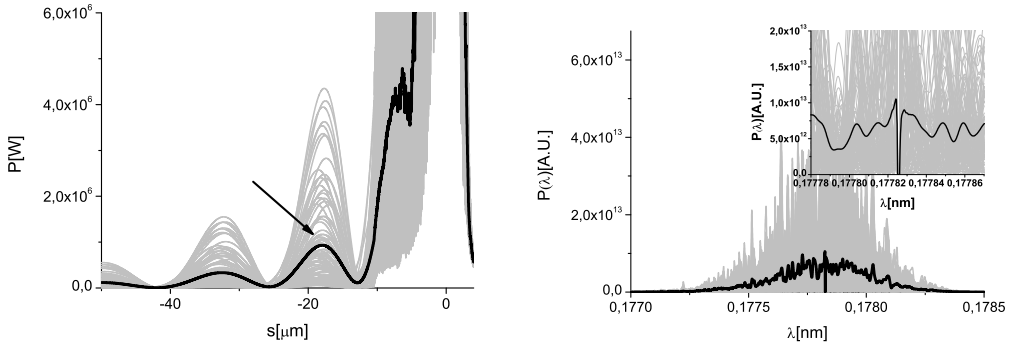

Fig. 32. Power and spectrum at 7 keV after the single crystal self-seeding X-ray monochromator. A 100 μm thick diamond crystal (C(113) Bragg reflection, σ-polarization) is used. Grey lines refer to single shot realizations, the black line refers to the average over a hundred realizations. The black arrow indicates the seeding region.

can identify the seed pulse. One the right side, before the FEL pulse, one has nominally zero power.

The seed is amplified up to saturation in the output undulator. As already discussed, we can use post-saturation tapering to increase the output power level. The tapering configuration in Fig. 34 is optimized for maximum output power level.

The output characteristics, in terms of power and spectrum, are shown in Fig. 35. The output power is increased of about a factor 20, allowing one to reach about one TW. The spectral width remains almost unvaried. The output level has been optimized by changing the tapering law, resulting in Fig. 34, and by changing the electron beam transverse size along the undulator, as suggested in [19]. Optimization was performed empirically. The evolution of the energy per pulse and of the energy fluctuations as a

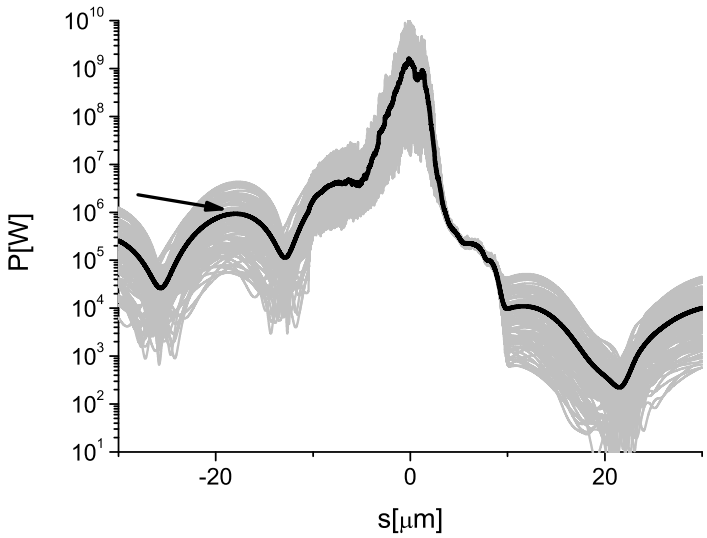

Fig. 33. Logarithmic plot of the power at 7 keV after the single crystal self-seeding X-ray monochromator. The black arrow indicates the seeding region. The region on the right hand side of the plot (before the FEL pulse) is nominally zero because of causality reasons. Differences with respect to zero give back the accuracy of our calculations.

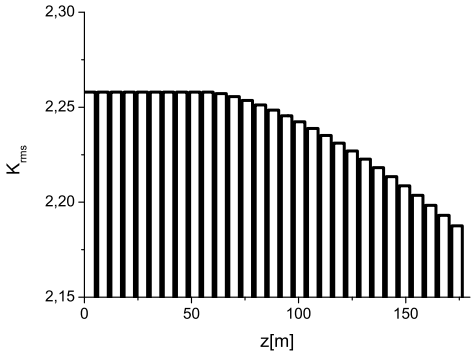

Fig. 34. Tapering law at 7 keV.

function of the undulator length are shown in Fig. 36. Finally, the transverse radiation distribution and divergence at the exit of the output undulator are shown in Fig. 37.

4.4 C(004) symmetric Bragg reflection at 8 keV

A feasibility study dealing with this energy range can be found in [6]. No changes are foreseen in this case.

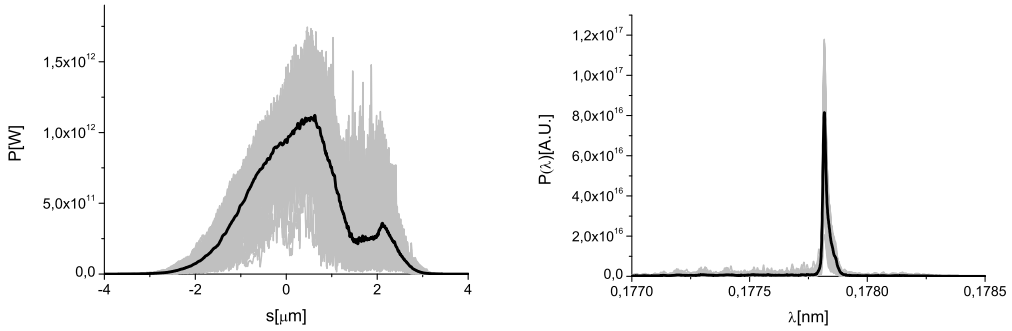

Fig. 35. Final output in the case of tapered output undulator at 7 keV. Power and spectrum are shown. Grey lines refer to single shot realizations, the black line refers to the average over a hundred realizations.

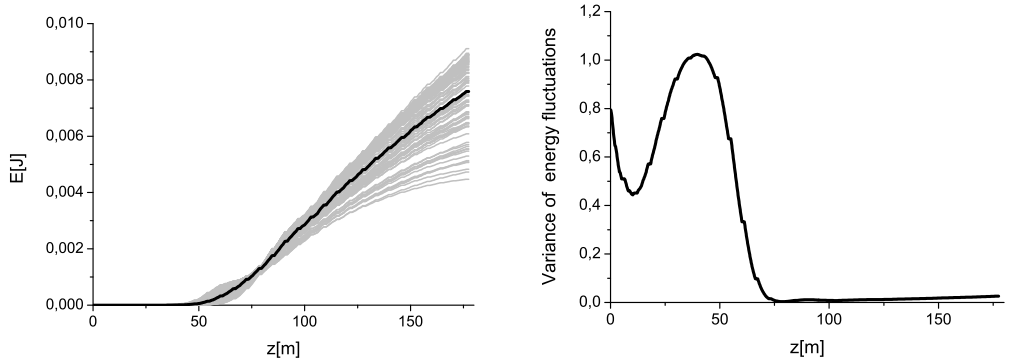

Fig. 36. Energy and energy variance of output pulses in the case of tapered output undulator at 7 keV. In the left plot, grey lines refer to single shot realizations, the black line refers to the average over a hundred realizations.

4.5 C(333) asymmetric Bragg reflection at 9 keV

Finally, we consider the energy point at 9 keV, which relies on the C(333) asymmetric Bragg reflection. Again, the first two magnetic chicanes are switched off. The electron beam lases in SASE mode along the first 11 undulator cells before passing through the single-crystal monochromator filter. Input power and spectrum are shown in Fig. 38

The effect of the filtering process is illustrated, both in the time and in the frequency domain, in Fig. 39.

The numerical accuracy with which causality is satisfied in our simulations can be shown by a logarithmic plot of the FEL pulse power after the crystal, Fig. 40. The peak in the center is the main FEL pulse. On the left side one can identify the seed pulse. One the right side, before the FEL pulse, one

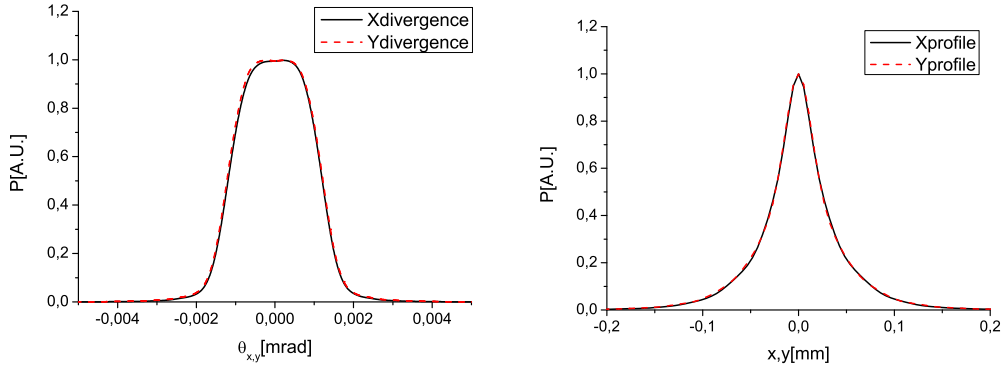

Fig. 37. Final output. X-ray radiation pulse energy distribution per unit surface and angular distribution of the X-ray pulse energy at 7 keV at the exit of output undulator.

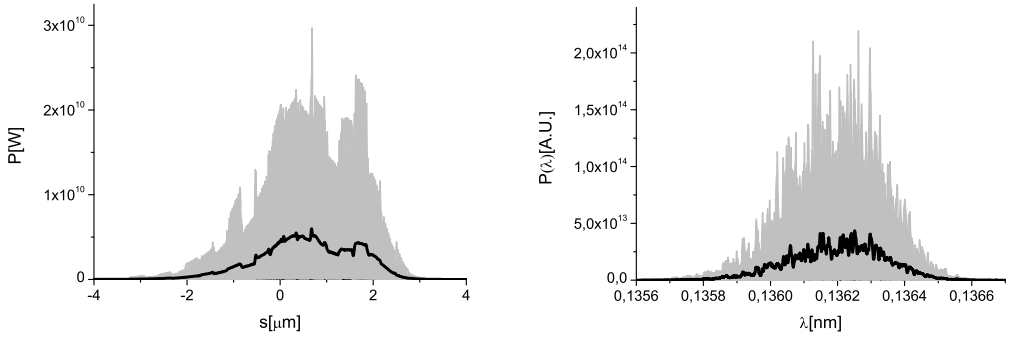

Fig. 38. Power and spectrum at 9 keV before the third magnetic chicane. Grey lines refer to single shot realizations, the black line refers to the average over a hundred realizations.

has nominally zero power.

The seed is amplified up to saturation in the output undulator. As already discussed, we can use post-saturation tapering to increase the output power level. The tapering configuration in Fig. 41 is optimized for maximum output power level.

The output characteristics, in terms of power and spectrum, are shown in Fig. 42. The output power is increased of about a factor 20, allowing one to reach about one TW. The spectral width remains almost unvaried. The output level has been optimized by changing the tapering law, resulting in Fig. 41, and by changing the electron beam transverse size along the undulator, as suggested in [19]. Optimization was performed empirically. The evolution of the energy per pulse and of the energy fluctuations as a function of the undulator length are shown in Fig. 43. Finally, the transverse radiation distribution and divergence at the exit of the output undulator are

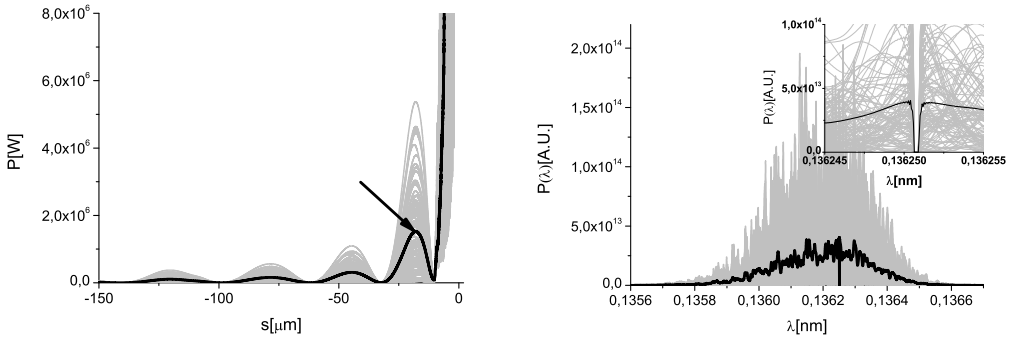

Fig. 39. Power and spectrum at 9 keV after the single crystal self-seeding X-ray monochromator. A 100 μm thick diamond crystal (C(333) Bragg reflection, σ-polarization) is used. Grey lines refer to single shot realizations, the black line refers to the average over a hundred realizations. The black arrow indicates the seeding region.

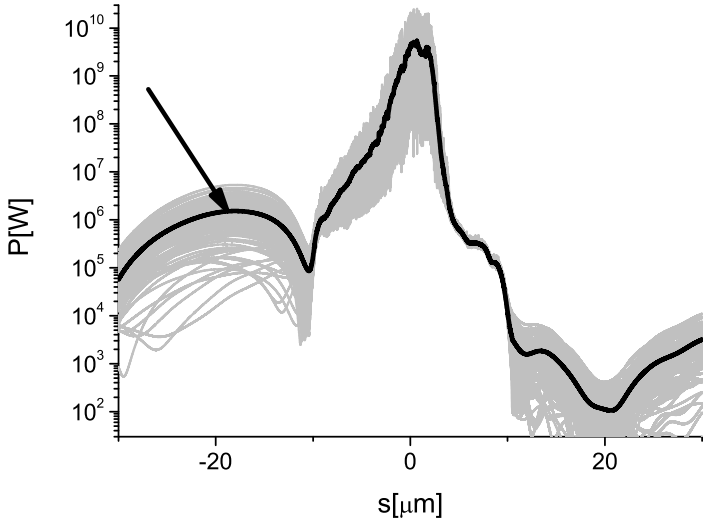

Fig. 40. Logarithmic plot of the power at 9 keV after the single crystal self-seeding X-ray monochromator. The black arrow indicates the seeding region. The region on the right hand side of the plot (before the FEL pulse) is nominally zero because of causality reasons. Differences with respect to zero give back the accuracy of our calculations.

shown in Fig. 44.

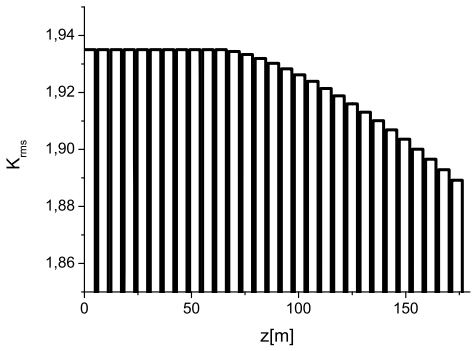

Fig. 41. Tapering law at 9 keV.

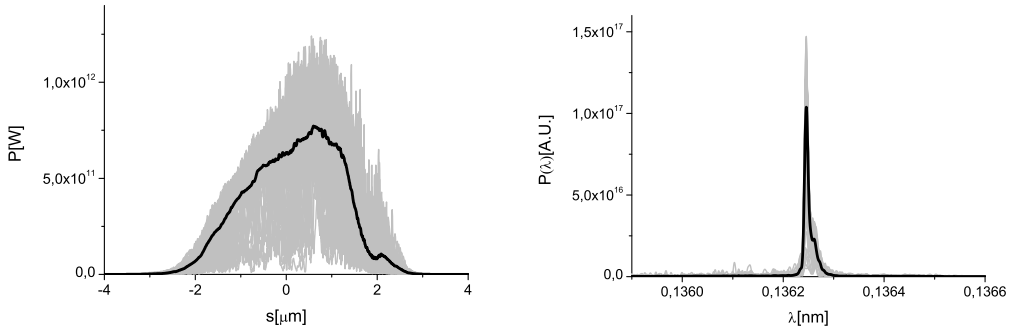

Fig. 42. Final output in the case of tapered output undulator at 9 keV. Power and spectrum are shown. Grey lines refer to single shot realizations, the black line refers to the average over a hundred realizations.

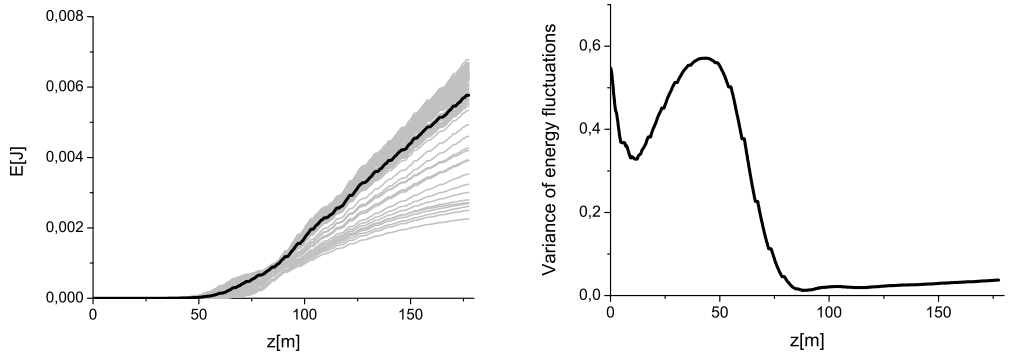

Fig. 43. Energy and energy variance of output pulses in the case of tapered output undulator at 9 keV. In the left plot, grey lines refer to single shot realizations, the black line refers to the average over a hundred realizations.

5 Conclusions

Self-seeding scheme with wake monochromators are routinely used in generation of narrow bandwidth X-ray pulses at LCLS [22]. Recently, the pho-

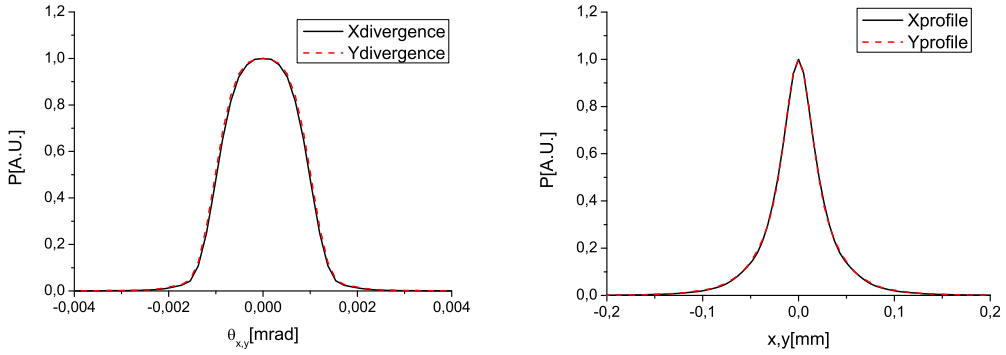

Fig. 44. Final output. X-ray radiation pulse energy distribution per unit surface and angular distribution of the X-ray pulse energy at 9 keV at the exit of output undulator.

ton energy range of self-seeding setup at LCLS was extended from 8 keV to lower photon energies down to 5.5 keV by exploiting different planes on the same diamond crystal [31].

In this article we propose a study of the performance of self-seeding setups for the European XFEL based on wake monochromators, exploiting different (symmetric and asymmetric, Bragg and Laue) reflections of a single diamond crystal, similar to that used into the LCLS setup. In our study we account the spatiotemporal shift of the seed induced by the passage through the crystal, and we study the dependence of the FEL input coupling factor on this shift. We exemplify our results using the concept for a dedicated bio-imaging beamline previously proposed by the authors. We conclude that crystals similar to the one actually used at the LCLS can be exploited to cover the energy range between 3 keV and 13 keV with high performance, allowing one to reach TW-class pulses.

6 Acknowledgements

We are grateful to Massimo Altarelli, Reinhard Brinkmann, Henry Chapman, Janos Hajdu, Viktor Lamzin, Serguei Molodtsov and Edgar Weckert for their support and their interest during the compilation of this work.

References

[1] J. Hajdu, Curr. Opin. Struct. Biol. 10, 569 (2000)
[2] R. Neutze et al., Nature 406, 752 (2000)
[3] K. J. Gaffney and H. N. Chapman, Science 316, 1444 (2007)

[4] M. M. Seibert et al., Nature 470 (7332) 78-81 (2011)
[5] S. Baradaran et al., LCLS-II New Instruments Workshops Report, SLAC-R-993 (2012), see Section 4.3.2. by H. Chapman et al., and Section 4.3.3. by F. R. N. C. Maia et al.
[6] G. Geloni, V. Kocharyan and E. Saldin, "Conceptual design of an undulator system for a dedicated bio-imaging beamline at the European X-ray FEL", DESY 12-082, http://arxiv.org/abs/1205.6345 (2012).
[7] G. Geloni, V. Kocharyan and E. Saldin, "Optimization of a dedicated bio-imaging beamline at the European X-ray FEL", DESY 12-159, http://arxiv.org/abs/1209.5972 (2012).
[8] J. Feldhaus et al., Optics. Comm. 140, 341 (1997).
[9] E. Saldin, E. Schneidmiller, Yu. Shvyd'ko and M. Yurkov, NIM A 475 357 (2001).
[10] E. Saldin, E. Schneidmiller and M. Yurkov, NIM A 445 178 (2000).
[11] R. Treusch, W. Brefeld, J. Feldhaus and U Hahn, Ann. report 2001 "The seeding project for the FEL in TTF phase II" (2001).
[12] A. Marinelli et al., Comparison of HGHG and Self Seeded Scheme for the Production of Narrow Bandwidth FEL Radiation, Proceedings of FEL 2008, MOPPH009, Gyeongju (2008).
[13] G. Geloni, V. Kocharyan and E. Saldin, "Scheme for generation of highly monochromatic X-rays from a baseline XFEL undulator", DESY 10-033 (2010).
[14] Geloni, G., Kocharyan V., and Saldin, E., "A novel Self-seeding scheme for hard X-ray FELs", Journal of Modern Optics, vol. 58, issue 16, pp. 1391-1403, DOI:10.1080/09500340.2011.586473 (2011)
[15] G. Geloni, V. Kocharyan and E. Saldin, "Scheme for generation of fully coherent, TW power level hard x-ray pulses from baseline undulators at the European XFEL", DESY 10-108 (2010).
[16] Geloni, G., Kocharyan, V., and Saldin, E., "Production of transform-limited X-ray pulses through self-seeding at the European X-ray FEL", DESY 11-165 (2011).
[17] W.M. Fawley et al., Toward TW-level LCLS radiation pulses, TUOA4, to appear in the FEL 2011 Conference proceedings, Shanghai, China, 2011
[18] J. Wu et al., Simulation of the Hard X-ray Self-seeding FEL at LCLS, MOPB09, to appear in the FEL 2011 Conference proceedings, Shanghai, China, 2011
[19] Y. Jiao et al. Phys. Rev. ST Accel. Beams 15, 050704 (2012)
[20] A. Authier, Dynamical Theory of X-Ray Diffraction (Oxford University, 2001).
[21] S. Bajit, H. Chapman, A. Aquila and E. Gullikson, J. Opt. Soc. Am. A, 29, 3, p. 216 (2012).
[22] J. Amann et al., Nature Photonics, DOI:10.1038/NPHOTON.2012.180 (2012).
[23] R. R. Lindberg and Yu.V. Shvydko, Phys. Rev. ST Accel. Beams 15,

100702 (2012).
[24] V. Lucarini et al., Kramers-Kronig relations in optical materials research, Springer, (2004).
[25] H. A. Kramers, La diffusion de la lumiere par les atomes, in Atti del Congresso Internazionale dei Fisici, Vol. 2 (Zanichelli, Bologna, 1927), pp. 545 557.
[26] R. de L. Kronig, On the theory of dispersion of x-rays, J. Opt. Soc. Am. 12, 547557 (1926).
[27] J. Toll, Phys. Rev. 104, 6 (1956).
[28] G. Geloni, V. Kocharyan and E. Saldin, "Pulse-front tilt caused by the use of a grating monochromator and self-seeding of soft X-ray FELs", DESY 12-051 (2012)
[29] S Reiche et al., Nucl. Instr. and Meth. A 429, 243 (1999).
[30] I. Zagorodnov, Private communication
[31] R. Lindberg et al., Hard X-ray Self-seeding at the LCLS, TUOAI02, to be published in the Proceedings of the FEL 2012 conference, Nara, Japan.